

Surface Acoustic Microwave Photonic Filters on Etchless Lithium Niobate Integrated Platform

Yue Yu and Xiankai Sun*

Lithium niobate on insulator emerges as a promising platform for integrated microwave photonics because of its capability of ultralow-loss guidance and high-efficiency modulation of light. Chip-level integration of microwave filters is important for signal processing in the 5G/6G wireless communication. Here, by employing bound states in the continuum for low-loss waveguiding, high-performance microwave photonic filters are realized on an etchless lithium niobate integrated platform. These microwave photonic filters consist of a high-quality photonic microcavity modulated by piezoelectrically excited surface acoustic waves. Acoustic time delays from 21 to 106 ns and passbands with bandwidth as narrow as 0.89 MHz are achieved in the fabricated filters operating at gigahertz frequencies. This demonstration may open up new applications on the lithium niobate integrated platform, such as optical communication, signal processing, and beam steering.

1. Introduction

Integrated microwave photonics (MWP) by combining photonic integrated circuit technology with MWP has shown its advantages in enhanced functionalities and robustness as well as reduced size, weight, cost, and power consumption. Microwave filtering is one of the most important functionalities in integrated MWP for signal processing in the 5G/6G wireless communication,^[1,2] which separates signals of interest from the noise background and mitigates unwanted interference.^[3] A common way for implementing integrated MWP filters is constructing multistage delay lines on a chip,^[4–6] where the input signal is discretely sampled, delayed, and weighted before being summed up. For applications that require narrow linewidths and/or free spectral ranges (FSRs), long time delays become necessary, leading to large footprints and high losses. Hyper-sonic acoustic waves with significantly lower velocity than optical waves can be adopted for overcoming this difficulty and obtaining the required long time delays within a small footprint.

Y. Yu, X. Sun
Department of Electronic Engineering
The Chinese University of Hong Kong
Shatin, New Territories, Hong Kong
E-mail: xksun@cuhk.edu.hk

 The ORCID identification number(s) for the author(s) of this article can be found under <https://doi.org/10.1002/lpor.202300385>

© 2024 The Authors. Laser & Photonics Reviews published by Wiley-VCH GmbH. This is an open access article under the terms of the [Creative Commons Attribution](#) License, which permits use, distribution and reproduction in any medium, provided the original work is properly cited.

DOI: 10.1002/lpor.202300385

One way of harnessing the acoustic waves for high-resolution filtering relies on the stimulated Brillouin scattering between guided light and sound waves, usually in nonsuspended chalcogenide glasses^[7,8] or suspended silicon membranes.^[9–11] Another type of sound waves, surface acoustic waves (SAWs) propagate at the surface of a material within a depth on the order of acoustic wavelength. SAWs have very high energy confinement and can attain large overlap with the optical mode of a planar waveguide on integrated platform, and thus have been widely applied in the areas of quantum communication,^[12] sensing,^[13,14] and signal processing.^[15–17] More importantly, tunable SAW devices have been

achieved recently by using mechanical nonlinear deformations,^[18] piezoelectrically actuated deformations,^[19] electroacoustic effects,^[20] and thermoacoustic effects^[21] at gigahertz frequencies. Therefore, SAW devices are an excellent candidate for high-resolution tunable MWP filters for next-generation wireless communication.

To date, most of the integrated MWP components are realized on mature material platforms including indium phosphide,^[22–24] silicon on insulator,^[16,17,25] and silicon nitride on insulator.^[26–28] Lithium niobate on insulator (LNOI) emerged as a new and promising platform for MWP due to the advantages of ultra-broad optical transparency window (350–5200 nm), strong piezoelectric effect, and large second-order optical nonlinearity.^[29,30] Moreover, the state-of-the-art lithium niobate integrated photonics technology supports ultralow-loss light propagation, thus enabling high-performance nonlinear applications in a wide wavelength range. All these advantages will lead to lower energy consumption, more compact footprint, and higher integration scale required for the next-generation optoelectronic chips, which pave the way for the 5G/6G communication. Photonic integrated circuits fabricated with etching processes rely on the development of etching recipes to achieve smooth vertical etched sidewalls, which are not yet available for many optical functional materials. Here, we adopted a fundamentally new photonic architecture by patterning a fabrication-friendly optically transparent material on a thin-film substrate without etching the substrate.^[31,32] This architecture features easy fabrication processes and excellent device performance, and has enabled various photonic functionalities on the LNOI platform, including 2D-material integration,^[33,34] high-dimensional communication,^[35] and second-harmonic generation,^[36] with performance comparable with those fabricated by etching the lithium niobate.

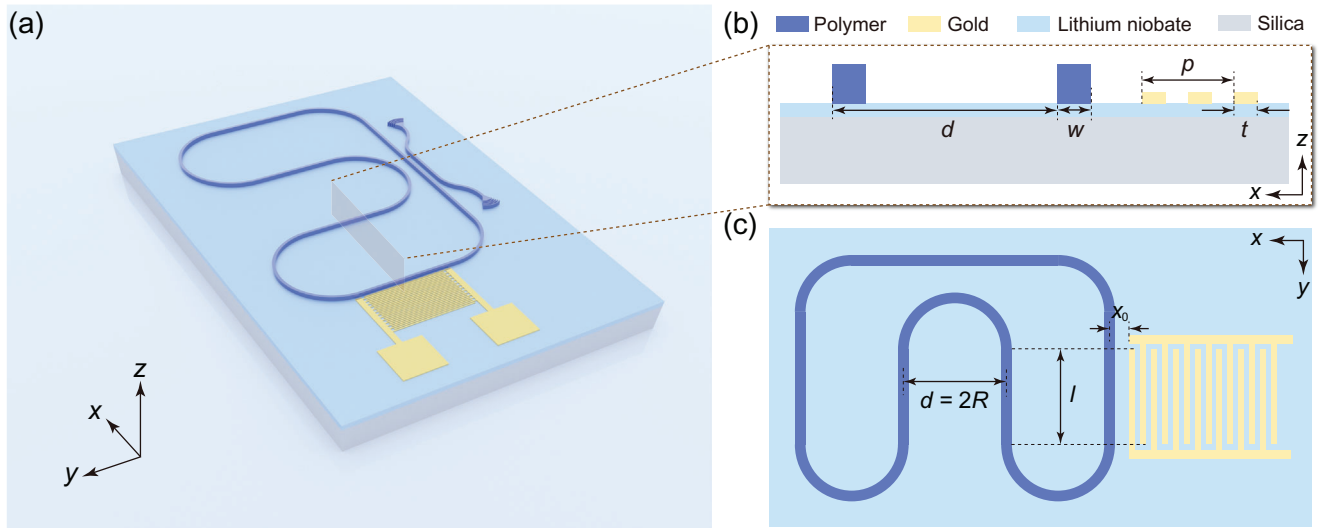


Figure 1. a) Illustration of the surface acoustic MWP filter on etchless LNOI platform. b) Cross-sectional view of the acousto-optic modulation region near the IDT. The dark blue part denotes the polymer waveguide, the yellow part denotes the IDT made of gold, the light blue part denotes the lithium niobate layer, and the gray part denotes the buried silicon oxide. w , d , p , and t represent the width of the polymer waveguide, the distance between adjacent taps, the period of the IDT, and the width of the IDT fingers, respectively. c) Top view of the photonic microcavity and IDT, where x_0 , d , and l denote the distance between the IDT and the first tap, the distance between adjacent taps, and the aperture of the IDT, respectively.

Moreover, due to the very different acoustic properties between polymer and lithium niobate, the SAWs can propagate in the unetched lithium niobate layer across the optical waveguides with negligible reflection or scattering, which is ideal for acousto-optic modulation.^[37,38] Here, by monolithically integrating an interdigital transducer (IDT) with a multitap photonic microcavity, we demonstrated high-resolution MWP filters on an etchless LNOI integrated platform for signal processing. The demonstrated filters can be scaled for operation in a wide frequency range from megahertz to tens of gigahertz, which will contribute to the development of high-performance MWP systems on the lithium niobate integrated platform.

2. Results and Discussion

Figure 1a illustrates the surface acoustic MWP filter fabricated on a z-cut LNOI substrate with an etchless process. We patterned a multitap photonic microcavity, where the taps consist of multiple equidistantly located straight waveguides joined by 180° bends, in a polymer (ZEP520A) on an LNOI substrate. An IDT was fabricated in the vicinity of an outermost tap for exciting the SAWs. To obtain maximal acousto-optic modulation, the IDT is oriented along the x direction by considering the anisotropic photoelastic coefficients of lithium niobate.^[39] Figure 1b shows the cross-section of the acousto-optic interaction region, where the thicknesses of the IDT gold electrodes, the lithium niobate layer, the polymer atop, and the silicon oxide underneath are 80 nm, 300 nm, 400 nm, and 2 μ m, respectively. w , d , p , and t represent the width of the polymer waveguide, the distance between adjacent taps, the period of the IDT, and the width of the IDT fingers, respectively. Figure 1c shows a top view of the photonic microcavity and IDT, where l is the aperture of the IDT and is also the length of the straight waveguide in a tap. An input microwave signal with frequency f was applied to the IDT to gener-

ate SAWs of the same frequency. When pf matches the velocity v of an SAW, the SAW can be excited and propagate away from the IDT (see Section S2, Supporting Information), which induces a phase modulation to light as it crosses a tap due to the acousto-optic effect. Considering that the typical velocity of SAWs is in the range of several thousand meters per second, an acoustic propagation length of hundreds of micrometers between adjacent taps induces a time delay of hundreds of nanoseconds. The phase modulation accumulated from N taps is converted to an intensity modulation at the output of the photonic microcavity. The impulse response of the MWP filter can be described by

$$h_R(t) = K \sum_{m=0}^{N-1} \exp\left(-\frac{\alpha}{2}mvT\right) \delta(t - mT), \quad (1)$$

where K is a prefactor that includes the efficiency of SAW excitation, acousto-optic modulation, and photodetection, α is the propagation loss coefficient of the SAW, and T is the unit acoustic delay equal to d/v (see Section S1, Supporting Information). The properties of the MWP filter are determined by the geometry of the photonic microcavity and the IDT. For example, a smaller FSR in the transfer function can be obtained by increasing the spacing between adjacent taps, a narrower bandwidth can be obtained by increasing the number of taps, the number of output passbands can be reduced by increasing the period of the IDT (see Section S1, Supporting Information). The surface acoustic MWP filters with design flexibility can facilitate microwave signal processing on the lithium niobate integrated photonic platform.

A major motivation for the MWP development is the low-loss transmission over long distances. The optical loss can have considerable effects on the system's performance, because it transforms into the microwave loss quadratically due to the square law in optical-to-electrical conversion by photodetectors.^[40]

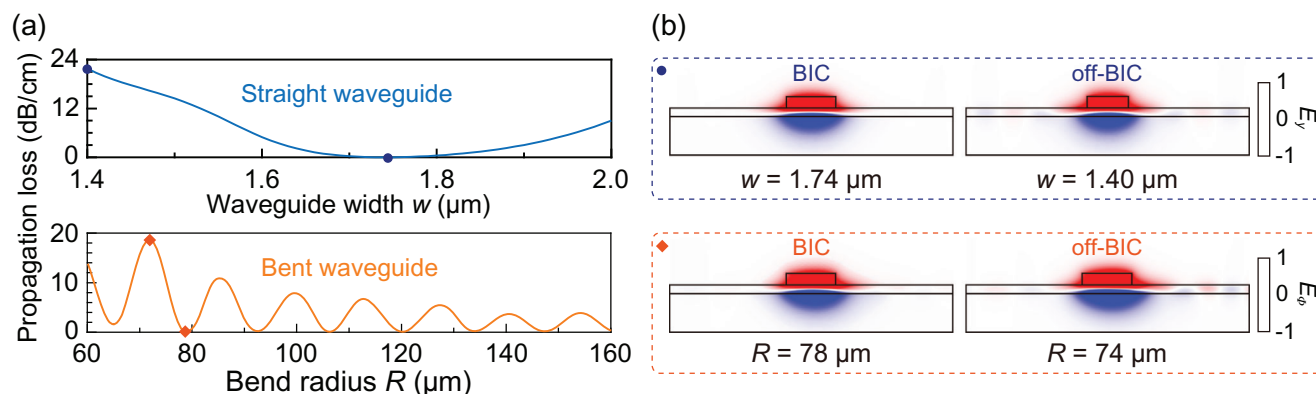


Figure 2. a) (Upper) Calculated propagation loss of a straight waveguide as a function of waveguide width w . (Lower) Calculated propagation loss of a bent waveguide as a function of bend radius R with fixed $w = 1.74$ μm. In both cases, the simulation was performed at the wavelength of 1510 nm. b) Modal profiles of the TM bound mode in a straight waveguide (upper) and in a bent waveguide (lower) at the BIC and off-BIC points marked in (a). E_y (E_ϕ) denotes the electric field component along the propagation direction of the straight (bent) waveguide.

Therefore, low-loss photonic integrated circuits are the foundation for constructing high-performance MWP filters on a chip. For a waveguide structure made of a low-refractive-index material on a high-reflective-index substrate as shown in Figure 1b, the TM-polarized bound mode lies in the TE-polarized continuous spectrum. Therefore, the TM bound mode can interact with the TE continuum, resulting in energy dissipation of the former. However, one can engineer the waveguide geometry to turn the TM bound mode into a bound state in the continuum (BIC) with completely eliminated energy dissipation.^[31] To obtain a high-quality photonic microcavity with multiple taps as shown in Figure 1a, one should minimize the waveguide propagation loss in all the straight and bent sections. The upper panel of Figure 2a shows that the propagation loss of the fundamental TM mode in a straight waveguide depends on the waveguide width w . A zero propagation loss can be achieved at $w = 1.74$ μm at the wavelength of 1510 nm. On the other hand, the propagation loss of the fundamental TM mode in a bent waveguide depends on both the waveguide width w and the bend radius R . The lower panel of Figure 2a plots the simulated propagation loss of the TM mode in a bent waveguide as a function of the bend radius R with $w = 1.74$ μm. When $R > 60$ μm, a zero propagation loss can be obtained at periodic R values ($R = 78, 92, 106$ μm ...). Figure 2b shows the modal profiles of the fundamental TM mode in a straight waveguide (upper) and a bent waveguide (lower) at the BIC and off-BIC points marked in Figure 2a. For the TM mode at the off-BIC point, there is obvious energy dissipation to the TE continuum. By contrast, the TM mode at the BIC point exhibits perfectly localized field, resulting in lossless propagation of photons in the continuum.

Based on the simulated results, we designed the multitap photonic microcavity by satisfying the BIC conditions for both straight and bent waveguides ($w = 1.74$ μm, $R = 134$ μm). The nearby IDT had $p = 2w = 3.48$ μm unless otherwise noted, to achieve maximal acousto-optic modulation efficiency. We fabricated the devices with an etchless process on a z-cut LNOI substrate. First, the IDT was fabricated with a lift-off process, which involved pattern definition by high-resolution electron-beam lithography and the subsequent gold deposition by electron-beam evaporation. Then, the polymer waveguides and microcav-

ity were fabricated with a second step of electron-beam lithography. Note that in this step the polymer on the SAWs' propagation path was also removed to avoid its possible attenuation effects on the SAWs. Figure 3a shows a top-view optical microscope image of a fabricated 4-tap device, and Figure 3b is a close-up view of its acousto-optic modulation region. We first measured the optical transmission of the photonic microcavity by coupling light into and out of the device via grating couplers. The input light was provided by a tunable semiconductor laser (Yenista T100S-HP) and the output light was collected by a photodetector (Hewlett Packard 81531A). Figure 3c plots the optical transmission spectrum of the device shown in Figure 3a. The zoomed-in spectrum in Figure 3d indicates loaded quality factors Q_L of $\approx 1.2 \times 10^5$ near the wavelength of 1510.0 nm. The factors preventing attainment of an even higher experimental Q_L may include waveguide sidewall roughness, material absorption, modal mismatch between the straight and bent sections of the microcavity, and waveguide deformation near the IDT.^[41] The Q_L can be further enhanced by optimizing the fabrication processes. For example, the waveguide sidewall roughness can be reduced by adding a baking step after lithographic patterning of the polymer. The material absorption can be reduced by replacing the polymer with another optically transparent material such as silicon oxide. The waveguide deformation near the IDT can be reduced by inverse compensation during the structural design. The measured optical FSR is 0.355 nm, which agrees well with the theoretical value of 0.358 nm obtained by using the cavity circumference of 2820 μm and the simulated group index of 2.253.

Figure 4a shows the experimental setup for characterizing microwave filtering of the fabricated devices. Light from the tunable semiconductor laser had its polarization adjusted by a fiber polarization controller before being coupled into the device via the input grating coupler. The laser wavelength was tuned to a maximal slope of the photonic microcavity's transmission spectrum. Meanwhile, a sinusoidal microwave signal from a vector network analyzer (Keysight E5071C) was delivered to the IDT via a microwave probe. The light inside the photonic microcavity experienced multiple times of acousto-optic modulation and was strongly enhanced near a cavity resonant wavelength. The light coupled out of the output grating coupler was split and collected

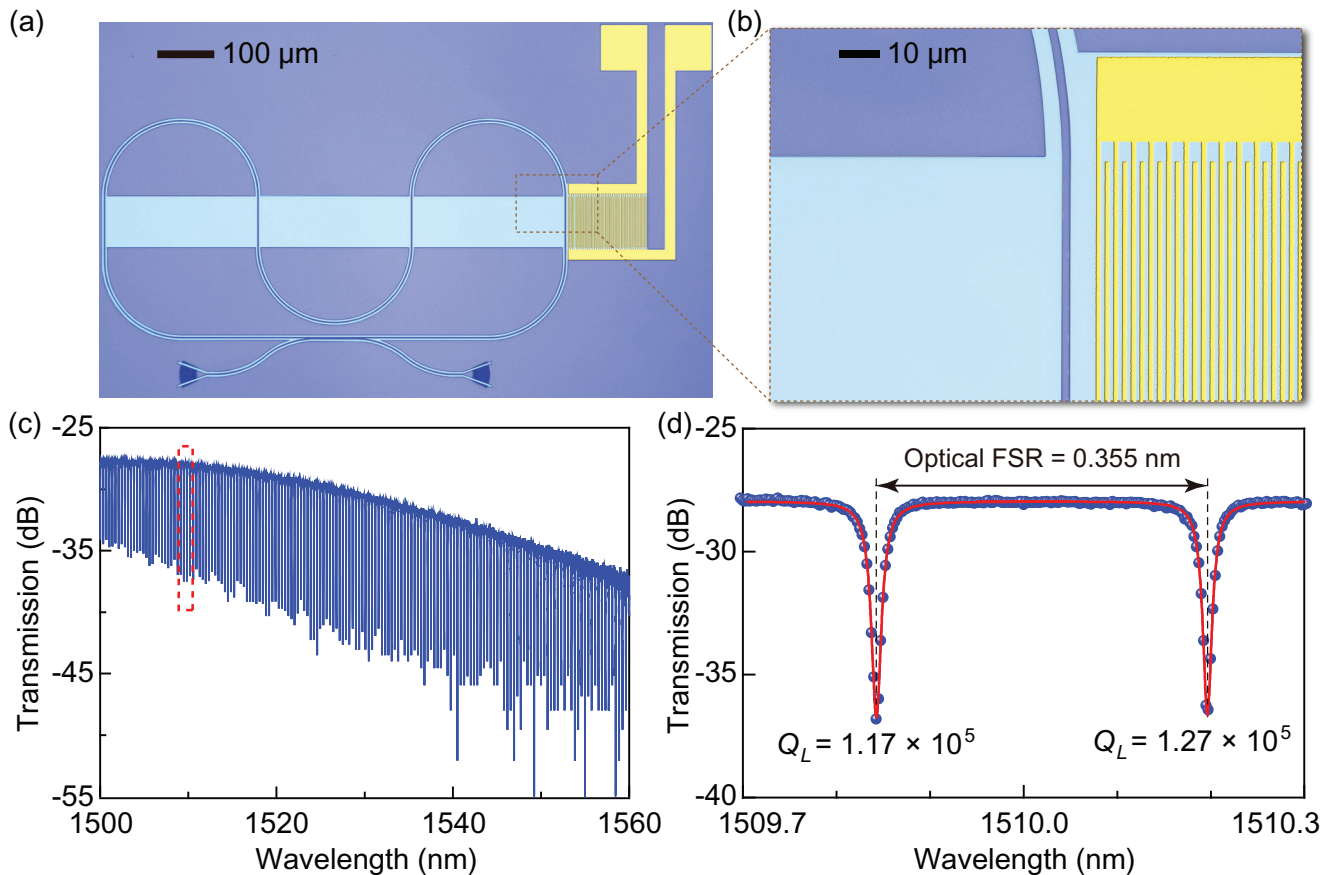


Figure 3. a) Optical microscope image of a fabricated 4-tap surface acoustic MWP filter. b) Close-up view of the acousto-optic modulation region. c) Measured optical transmission spectrum in a broad wavelength range. d) Zoomed-in optical transmission spectrum near 1510 nm. The blue dots represent the measured data and the red line is the corresponding Lorentzian fit.

by two photodetectors. A high-sensitivity photodetector (Hewlett Packard 81531A) was used to monitor the cavity transmission for tuning the laser wavelength. A high-speed photodetector (Optilab A1803) was used to convert the SAW-modulated light signals into the electrical domain, which were sent back to the vector network analyzer for obtaining the transfer function.

In Figure 4b, the measured $|S_{11}|$ spectrum shows several dips. To identify the excited SAW modes, we fabricated a series of devices with IDT finger period p varying from 2.6 to 4.2 μm . Figure 4c shows the simulated and measured frequencies of the SAW modes, which agree well with each other. The red dashed line marks the case in Figure 4b, where the IDT finger period is $p = 2w = 3.48 \mu\text{m}$, and the two red stars represent the measured frequencies at the two dips [0.78 GHz (①) and 1.60 GHz (②)]. Figure 4d shows the cross-sectional displacement field profiles (x component) of the two SAW modes. Based on the relationship between the IDT finger period and the excited SAW frequency in Figure 4c, we obtained the simulated velocity of SAW modes ① and ② as $v_1 = 2714 \text{ m s}^{-1}$ and $v_2 = 5398 \text{ m s}^{-1}$, respectively (see Section S2, Supporting Information).

Next, we characterized the microwave filtering performance of our fabricated devices. The incident microwave drive power was set as -5 dBm for all measurements. Figure 5a,b shows the measured normalized $|S_{21}|$ spectra of 4- and 6-tap surface acoustic

MWP filters with $d = 2R = 268 \mu\text{m}$ at frequencies near 0.78 and 1.60 GHz. These spectra exhibit periodic passbands with an FSR of 10.6 and 16.6 MHz, corresponding to an acoustic delay of 94.3 and 60.2 ns, respectively, over the propagation distance d . Additionally, the passband bandwidth decreases as the number of the taps increases, achieving the smallest full width at half maximum of 0.89 and 2.9 MHz, respectively. Figure 5c,d plots the normalized impulse response, derived from the measured complex-valued frequency response in Figure 5a,b, respectively. Exponential fits of the decaying amplitude of the impulse response in Figure 5c,d indicate the propagation loss α of 5.2 and 2.1 mm^{-1} for the SAW modes ① and ②, respectively.

Since the FSR of the passbands depends on both the SAW velocity v and the tap spacing d , we fabricated a series of 6-tap surface acoustic MWP filters with different tap spacings d , where $R = d/2$ satisfies the BIC condition for bent waveguides as shown in Figure 2a. We experimentally achieved time delays from 21 to 106 ns and measured the velocities of the two excited SAW modes as 2842 and 4904 m s^{-1} (see Section S2, Supporting Information). With these experimental results, we estimated the effective refractive index perturbation magnitude as $\Delta n_{\text{eff}} = 4.7 \times 10^{-6}$ RIU and the acousto-optic modulation depth as $M = 4.75\%$ (see Section S3, Supporting Information). These results can be further improved by optimizing the fabrication processes to reduce the

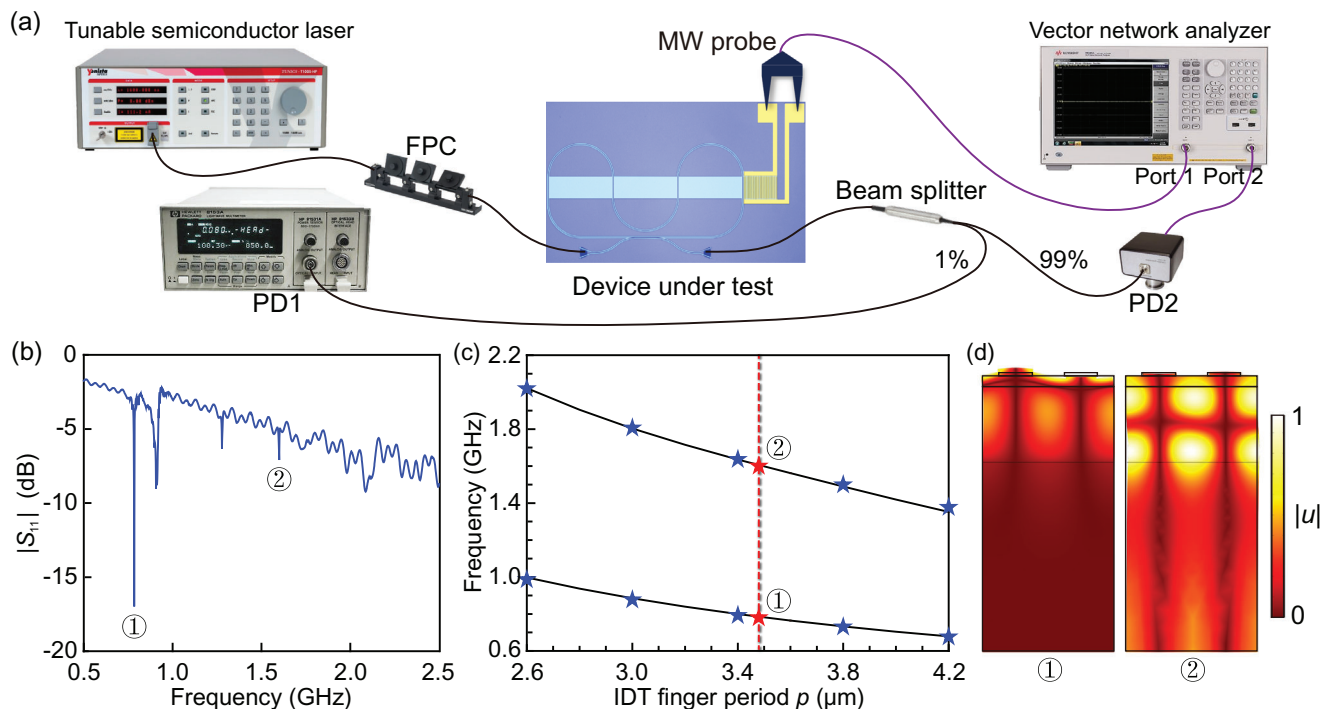


Figure 4. a) Experimental setup for measuring the acousto-optic modulation. MW probe, microwave probe; FPC, fiber polarization controller; PD1, high-sensitivity photodetector; PD2, high-speed photodetector. b) Measured $|S_{11}|$ spectrum for a device with the IDT finger period of $3.48 \mu\text{m}$. c) Simulated and measured frequencies of the two SAW modes as a function of the IDT finger period. The black solid lines plot the simulated results and the stars represent the experimentally measured data. The two red stars mark the frequencies of the two labeled SAW modes in (b). d) Simulated cross-sectional x-displacement profiles $|u|$ of the two labeled SAW modes in (b).

optical loss and by optimizing the IDT structure to enhance the SAW excitation efficiency.

Compared with the Brillouin-based MWP filters,^[42–44] where millimeter- or centimeter-long waveguide and milliwatt optical power are needed for producing sufficient stimulated Brillouin scattering (SBS) gain, our SAW-based MWP filters by utilizing the strong piezoelectric effect of lithium niobate can obtain a long delay time with a hundreds-of-micrometer-long acousto-optic modulation region and microwatt electrical power. Besides, since the SBS gain depends on the material's refractive index and elasticity, the Brillouin-based MWP filters are sensitive to fabrication processes and environmental temperature, thus having limited applications. Compared with the MWP filters on silicon-on-insulator platforms,^[16,17] which need hundreds-of-milliwatt optical power for stimulating SAWs and lack efficient tuning mechanisms, our SAW-based MWP filters can be tuned more easily by harnessing the excellent properties of lithium niobate. For example, the central frequency can be tuned by heating or cooling the device chip, and the delay time can be tuned by the electroacoustic and/or thermoacoustic effects.^[20,21] In addition, lithium niobate supports SAWs with a lower acoustic velocity ($\approx 4000 \text{ m s}^{-1}$) than that of silicon ($\approx 5000 \text{ m s}^{-1}$), and thus it is possible to obtain a longer delay time on the lithium niobate platform with the same device footprint.

Table 1 compares different types of MWP filters on integrated platforms. Here, the size refers to the effective length of optical waveguide. The link gain is defined as the ratio of the average RF output power to the average RF input power, which was ob-

tained directly from the network analyzer. Among all the integrated MWP filters, ours feature a high resolution, compact device footprint, and low energy consumption. However, our MWP filters exhibit a relatively low link gain. This is attributed mainly to the low optical pump power on the chip, which was limited by the input laser power and the grating couplers' loss in our experiment. This optical pump power can be increased substantially by using edge-coupling scheme and low-noise optical amplifier. Additionally, further optimization of the IDT structure should lead to more efficient acousto-optic modulation, thus reducing the passband bandwidth and increasing the link gain even further.

3. Conclusion

In conclusion, we have experimentally demonstrated surface acoustic MWP filters on an etchless lithium niobate integrated platform. The devices consist of a high-quality multitap photonic microcavity modulated by piezoelectrically excited surface acoustic waves. The devices operated under the principle of photonic bound states in the continuum for low-loss waveguiding and high-quality resonating and achieved high-performance in microwave filtering. We fabricated devices with 4 and 6 taps and realized an acoustic delay from 21 to 106 ns. Compared with other types of MWP filters based on Brillouin scattering and/or in a fiber-optic system, our surface acoustic MWP filters benefit from these competitive advantages: i) simple fabrication process which does not need etching of the substrate or suspen-

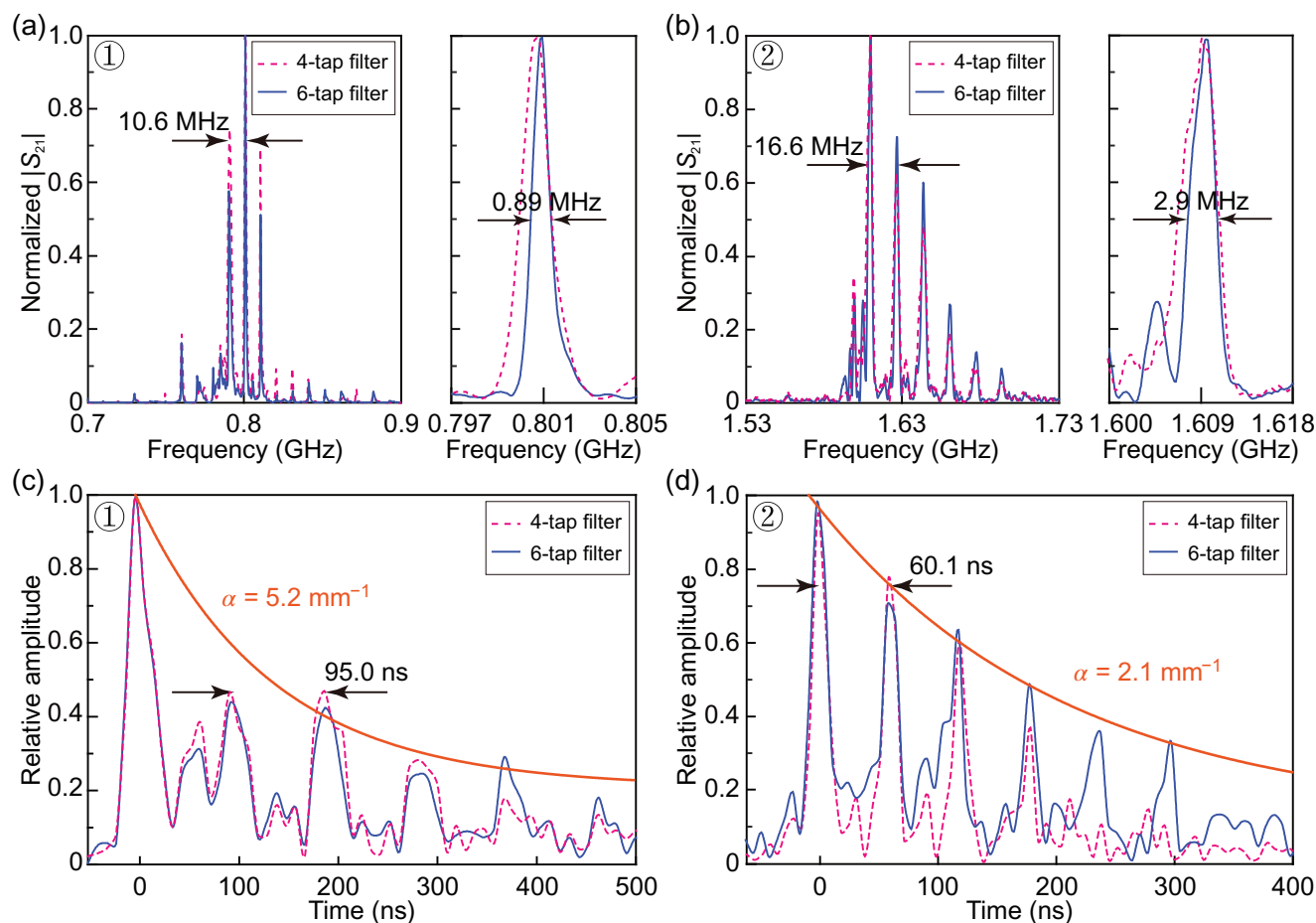


Figure 5. a,b) Measured normalized $|S_{21}|$ spectra for 4- and 6-tap surface acoustic MWP filters at frequencies near 0.78 GHz (a) and 1.60 GHz (b). The right figures show the zoomed-in spectra of the central peak, where a full width at half maximum of 0.89 and 2.9 MHz was obtained from the 6-tap filter. Here both the 4- and 6-tap filters have $d = 2R = 268 \text{ } \mu\text{m}$. c,d) Normalized impulse response, derived from the measured complex-valued frequency response in (a) and (b). The orange solid lines plot the corresponding exponential fits.

sion of delicate membranes or waveguides; ii) long time delay achieved within a small footprint due to the slow velocity of acoustic waves; iii) low energy consumption due to strong piezoelectric effect; iv) robustness against environmental perturbations such as vibrations and temperature gradients; v) easy ex-

tension of the microwave filtering concept to any other substrates and/or frequencies. With the superior properties of lithium niobate, the demonstrated surface acoustic MWP filters pave the way for a fully integrated MWP system on an LNOI chip, including light sources, amplifiers, modulators, signal processors, and

Table 1. Performance comparison of MWP filters on integrated platforms.

Platform	Type	Size	Center frequency [GHz]	Bandwidth [MHz]	Optical power [mW]	Link gain [dB]
GaInP ^[6]	Notch	1.5 mm	3–4	15	10	–45
InP ^[24]	Passband	4.0 mm	20	2500–5500	NA	–20
As ₂ S ₃ ^[8]	Passband	11.7 cm	3.6–30	140.0	40	22
			20.8	80.0		15
Suspended silicon ^[10]	Passband	5.0 cm	3.9	6.2	105	–17.3
As ₂ S ₃ on silicon ^[42]	Notch	6.5 cm	1.0–30	33–88	100	NA
As ₂ S ₃ on silicon ^[40]	Notch	2.6 cm	1–12	3	150	–30–10
Silicon on insulator ^[17]	Passband	2.4 mm	2.4	5	10–300	–104
Silicon nitride ^[28]	Notch	NA	5–20	400	NA	10
	Passband	NA	5–20	400	NA	1.2
This work	Passband	2.8 mm	0.8	0.89	18	–40

photodetectors, with significantly enhanced compactness and system stability.

Supporting Information

Supporting Information is available from the Wiley Online Library or from the author.

Acknowledgements

The authors would like to thank Mr. Piao Deng for his assistance with theoretical analysis. This work was supported by Research Grants Council of Hong Kong (No. 14206318, 14208421, C4050-21E) and The Chinese University of Hong Kong (Group Research Scheme).

Conflict of Interest

The authors declare no conflict of interest.

Data Availability Statement

The data that support the findings of this study are available from the corresponding author upon reasonable request.

Keywords

bound states in the continuum, lithium niobate, microwave photonic filters, surface acoustic waves, signal processing

Received: May 3, 2023
Revised: September 7, 2023
Published online: April 2, 2024

- [1] D. Marpaung, C. Roeloffzen, R. Heideman, A. Leinse, S. Sales, J. Capmany, *Laser Photon. Rev.* **2013**, *7*, 506.
- [2] D. Marpaung, J. Yao, J. Capmany, *Nat. Photonics* **2019**, *13*, 80.
- [3] V. J. Urick, K. J. Williams, J. D. McKinney, *Fundamentals of Microwave Photonics*, Wiley, Hoboken, NJ, USA, **2015**.
- [4] A. V. Oppenheim, *Discrete-Time Signal Processing*, Pearson Education India, Delhi, NCR, **1999**.
- [5] J. Capmany, B. Ortega, D. Pastor, *J. Lightwave Technol.* **2006**, *24*, 201.
- [6] J. Sancho, J. Bourderionnet, J. Lloret, S. Combrié, I. Gasulla, S. Xavier, S. Sales, P. Colman, G. Lehoucq, D. Dolfi, J. Capmany, A. De Rossi, *Nat. Commun.* **2012**, *3*, 1075.
- [7] B. Morrison, A. Casas-Bedoya, G. Ren, K. Vu, Y. Liu, A. Zarifi, T. G. Nguyen, D.-Y. Choi, D. Marpaung, S. J. Madden, A. Mitchell, B. J. Eggleton, *Optica* **2017**, *4*, 847.
- [8] A. Choudhary, I. Aryanfar, S. Shahnia, B. Morrison, K. Vu, S. Madden, B. Luther-Davies, D. Marpaung, B. J. Eggleton, *Opt. Lett.* **2016**, *41*, 436.
- [9] E. A. Kittlaus, P. Kharel, N. T. Otterstrom, Z. Wang, P. T. Rakich, *J. Lightwave Technol.* **2018**, *36*, 2803.
- [10] S. Gertler, E. A. Kittlaus, N. T. Otterstrom, P. T. Rakich, *APL Photonics* **2020**, *5*, 096103.
- [11] S. Gertler, E. A. Kittlaus, N. T. Otterstrom, P. Kharel, P. T. Rakich, *J. Lightwave Technol.* **2020**, *38*, 5248.
- [12] K. J. Satzinger, Y. P. Zhong, H.-S. Chang, G. A. Pears, A. Bienfait, M.-H. Chou, A. Y. Cleland, C. R. Conner, É. Dumur, J. Grebel, I. Gutierrez, B. H. November, R. G. Povey, S. J. Whiteley, D. D. Awschalom, D. I. Schuster, A. N. Cleland, *Nature* **2018**, *563*, 661.
- [13] J. Zhou, J. Zheng, X. Shi, Z. Chen, J. Wu, S. Xiong, J. Luo, S. Dong, H. Jin, H. Duan, Y. Fu, *J. Electrochem. Soc.* **2019**, *166*, B432.
- [14] Y.-S. Choi, J. Lee, Y. Lee, J. Kwak, S. Suk Lee, *Appl. Phys. Lett.* **2018**, *113*, 083702.
- [15] J. D. Maines, E. G. S. Paige, *Proc. IEEE* **1976**, *64*, 639.
- [16] D. Munk, M. Katzman, M. Hen, M. Priel, M. Feldberg, T. Sharabani, S. Levy, A. Bergman, A. Zadok, *Nat. Commun.* **2019**, *10*, 4214.
- [17] M. Katzman, D. Munk, M. Priel, E. Grunwald, M. Hen, N. Inbar, M. Feldberg, T. Sharabani, R. Zektzer, G. Bashan, M. Vofsi, U. Levy, A. Zadok, *Optica* **2021**, *8*, 697.
- [18] D. Hatanaka, I. Mahboob, K. Onomitsu, H. Yamaguchi, *Nat. Nanotechnol.* **2014**, *9*, 520.
- [19] J. C. Taylor, E. Chatterjee, W. F. Kindel, D. Soh, M. Eichenfield, *npj Quantum Inform.* **2022**, *8*, 19.
- [20] L. Shao, Di Zhu, M. Colangelo, D. Lee, N. Sinclair, Y. Hu, P. T. Rakich, K. Lai, K. K. Berggren, M. Loncar, *Nat. Electron.* **2022**, *5*, 348.
- [21] L. Shao, S. W. Ding, Y. Ma, Y. Zhang, N. Sinclair, M. Loncar, *Phys. Rev. Appl.* **2022**, *18*, 054078.
- [22] M. Smit, X. Leijtens, H. Ambrosius, E. Bente, J. Van Der Tol, B. Smalbrugge, T. De Vries, E.-J. Geluk, J. Bolck, R. Van Veldhoven, L. Augustin, P. Thijs, D. D'agostino, H. Rabbani, K. Lawniczuk, S. Stopinski, S. Tahvili, A. Corradi, E. Kleijn, D. Dzibrou, M. Felicetti, E. Bitincka, V. Moskalenko, J. Zhao, R. Santos, G. Gilardi, W. Yao, K. Williams, P. Stabile, P. Kuindersma, et al., *Semicond. Sci. Technol.* **2014**, *29*, 083001.
- [23] L. A. Coldren, S. C. Nicholes, L. Johansson, S. Ristic, R. S. Guzzon, E. J. Norberg, U. Krishnamachari, *J. Lightwave Technol.* **2011**, *29*, 554.
- [24] J. S. Fandiño, P. Muñoz, D. Doménech, J. Capmany, *Nat. Photonics* **2017**, *11*, 124.
- [25] C. Zhang, S. Zhang, J. D. Peters, J. E. Bowers, *Optica* **2016**, *3*, 785.
- [26] C. G. H. Roeloffzen, L. Zhuang, C. Taddei, A. Leinse, R. G. Heideman, P. W. L. Van Dijk, R. M. Oldenbeuving, D. A. I. Marpaung, M. Burla, K.-J. Boller, *Opt. Express* **2013**, *21*, 22937.
- [27] D. J. Moss, R. Morandotti, A. L. Gaeta, M. Lipson, *Nat. Photonics* **2013**, *7*, 597.
- [28] O. Daulay, G. Liu, K. Ye, R. Botter, Y. Klaver, Q. Tan, H. Yu, M. Hoekman, E. Klein, C. Roeloffzen, Y. Liu, D. Marpaung, *Nat. Commun.* **2022**, *13*, 7798.
- [29] G. Poberaj, H. Hu, W. Sohler, P. Günter, *Laser Photon. Rev.* **2012**, *6*, 488.
- [30] A. Boes, B. Corcoran, L. Chang, J. Bowers, A. Mitchell, *Laser Photon. Rev.* **2018**, *12*, 1700256.
- [31] C.-L. Zou, J.-M. Cui, F.-W. Sun, X. Xiong, X.-B. Zou, Z.-F. Han, G.-C. Guo, *Laser Photon. Rev.* **2015**, *9*, 114.
- [32] Z. Yu, X. Xi, J. Ma, H. Ki Tsang, C.-L. Zou, X. Sun, *Optica* **2019**, *6*, 1342.
- [33] Y. Wang, Z. Yu, Z. Zhang, B. Sun, Y. Tong, J.-B. Xu, X. Sun, H. K. Tsang, *ACS Photonics* **2020**, *7*, 2643.
- [34] Z. Yu, Y. Wang, B. Sun, Y. Tong, J.-B. Xu, H. Ki Tsang, X. Sun, *Adv. Opt. Mater.* **2019**, *7*, 1901306.
- [35] Z. Yu, Y. Tong, H. K. Tsang, X. Sun, *Nat. Commun.* **2020**, *11*, 2602.
- [36] F. Ye, Y. Yu, X. Xi, X. Sun, *Laser Photon. Rev.* **2022**, *16*, 2100429.
- [37] Z. Yu, X. Sun, *Light Sci. Appl.* **2020**, *9*, 1.
- [38] Z. Yu, X. Sun, *ACS Photonics* **2021**, *8*, 798.
- [39] J. Xu, R. Stroud, *Acousto-Optic Devices: Principles, Design, and Applications*, Wiley, Hoboken, NJ, USA **1992**.
- [40] Y. Liu, A. Choudhary, D. Marpaung, B. J. Eggleton, *Adv. Opt. Photonics* **2020**, *12*, 485.
- [41] Y. Yu, L. Wang, X. Sun, *Nanophotonics* **2021**, *10*, 4323.
- [42] Y. Liu, A. Choudhary, G. Ren, K. Vu, B. Morrison, A. Casas-Bedoya, T. G. Nguyen, D.-Y. Choi, P. Ma, A. Mitchell, S. J. Madden, D. Marpaung, B. J. Eggleton, *APL Photonics* **2019**, *4*, 106103.
- [43] D. Marpaung, B. Morrison, M. Pagani, R. Pant, D.-Y. Choi, B. Luther-Davies, S. J. Madden, B. J. Eggleton, *Optica* **2015**, *2*, 76.
- [44] Y. Xie, A. Choudhary, Y. Liu, D. Marpaung, K. Vu, P. Ma, D.-Y. Choi, S. Madden, B. J. Eggleton, *J. Lightwave Technol.* **2019**, *37*, 5246.